

Monoclinic *Cc*-phase stabilization in magnetically diluted lead free  $\text{Na}_{1/2}\text{Bi}_{1/2}\text{TiO}_3$ —Evolution of spin glass like behavior with enhanced ferroelectric and dielectric properties

This content has been downloaded from IOPscience. Please scroll down to see the full text.

View [the table of contents for this issue](#), or go to the [journal homepage](#) for more

Download details:

IP Address: 142.66.3.42

This content was downloaded on 26/09/2015 at 08:30

Please note that [terms and conditions apply](#).

## Materials Research Express



## PAPER

Monoclinic  $Cc$ -phase stabilization in magnetically diluted lead free  $\text{Na}_{1/2}\text{Bi}_{1/2}\text{TiO}_3$ —Evolution of spin glass like behavior with enhanced ferroelectric and dielectric propertiesRECEIVED  
23 April 2015REVISED  
9 July 2015ACCEPTED FOR PUBLICATION  
28 July 2015PUBLISHED  
1 September 2015Karthik Thangavelu<sup>1,2</sup> and Saket Asthana<sup>1</sup><sup>1</sup> Advanced Functional Materials Laboratory, Department of Physics, Indian Institute of Technology Hyderabad-502205, Telangana, India<sup>2</sup> Department of Materials Science and Metallurgical Engineering, Indian Institute of Technology Hyderabad -502205, Telangana, IndiaE-mail: [asthanas@iith.ac.in](mailto:asthanas@iith.ac.in)**Keywords:** structural phase stabilization, diluted magnetic ferroelectric, dielectrics, magnetic properties**Abstract**

The effect of magnetic cation substitution on the phase stabilization, ferroelectric, dielectric and magnetic properties of a lead free  $\text{Na}_{0.5}\text{Bi}_{0.5}\text{TiO}_3$  (NBT) system prepared by  $\text{O}_2$  atmosphere solid state sintering were studied extensively. Cobalt (Co) was chosen as the magnetic cation to substitute at the Ti-site of NBT with optimized 2.5 mol%. Rietveld analysis of x-ray diffraction data favours the monoclinic  $Cc$  phase stabilization strongly rather than the parent  $R3c$  phase. FE-SEM micrograph supports the single phase characteristics without phase segregation at the grain boundaries. The stabilized  $Cc$  space group was explained based on the collective local distortion effects due to spin-orbit stabilization at  $\text{Co}^{3+}$  and  $\text{Co}^{2+}$  functional centres. The phonon mode changes as observed in the  $\text{TiO}_6$  octahedral modes also support the  $Cc$  phase stabilization. The major  $\text{Co}^{3+}$ -ion presence was revealed from corresponding crystal field transitions observed through solid state diffuse reflectance spectroscopy. The enhanced spontaneous polarization ( $P_s$ ) from  $\cong 38 \mu\text{C cm}^{-2}$  to  $45 \mu\text{C cm}^{-2}$  could be due to the easy rotation of polarization vector along the  $(1\bar{1}0)_{\text{pc}}$  in  $Cc$  phase. An increase in static dielectric response ( $\epsilon$ ) from  $\epsilon \cong 42$  to 60 along with enhanced diffusivity from  $\gamma \cong 1.53$  to 1.75 was observed. Magneto-thermal irreversibility and their magnetic field dependent ZFC/FC curves suggest the possibility of a spin glass like behaviour below 50 K. The monoclinic  $Cc$  phase stabilization as confirmed from structural studies was well correlated with the observed ferroic properties in magnetically diluted NBT.

**1. Introduction**

$\text{Na}_{0.5}\text{Bi}_{0.5}\text{TiO}_3$  (NBT) is one among the promising lead free ferro/piezoelectric materials, which has been well studied in recent years because of its interesting structural diversity [1–3] and electromechanical properties [4]. Recently, several reports show that substitution of a magnetically active transition metal cation in a ferroelectric oxide could show magnetoelectric coupling [5–8]. Among them, site specific Mn substituted  $\text{SrTiO}_3$  and  $\text{KTaO}_3$  systems exhibited a multi-glass state which has been coupled magneto-electrically at low temperatures [5–8]. However, the processing conditions play a prominent role to avoid ambiguities related to parasitic effects such as magnetic phase separation [8–10]. There are few reports existing with magnetic cation substitution such as Fe, Mn and very few with Co substituted NBT systems. Aksel *et al* showed that addition of Fe (0–2 at.%) to NBT undergoes no structural transition; however addition of 0.5 and 1.0 at.% led to an increase in the depolarization temperature ( $T_d$ ) followed by a slight decrease with the addition of higher Fe content [11]. Similarly, Davies *et al* observed enhanced temperature stability in the  $T_d$  region with enhanced piezoelectric properties in the case of 0.5 at.% Mn/Fe substitution in NBT [12]. Aksel *et al* observed that  $\text{Fe}_2\text{O}_3$  doping leads to the formation of  $\text{Fe}^{3+}$  functional centre at Ti-site of the NBT lattice and promotes moderate hardening for 1 mol% doping concentration [13]. In Mn (1 at.%) substituted NBT single crystal, the correlation length of polar regions increased from 38 nm to 78 nm [14]. The selected area electron diffraction (SAED) showed that Mn substitution

favoured coexisting  $1/2\{ooo\}$  ( $o$ — stands for odd integer) and  $1/2\{oe\}$  ( $e$ — stands for even integer) types of oxygen octahedral tilt systems, whereas only  $1/2\{oe\}$  type tilt system is observed for pure NBT by Yao *et al* [14]. In addition, Ge *et al* observed that Mn (0.24 at.%) substitution in NBT single crystal enhances the ferroelectric ( $P_r = 23.9 \mu\text{C cm}^{-2}$ ), dielectric and piezoelectric ( $d_{33} = 120 \text{ pC/N}$ ) properties [15]. Also, the phase transition sequence of NBT is unaltered by Mn substitution. However, a decrease in the ferroelastic domain size by a factor of less than 2 was found due to Mn substitution [15]. Wang *et al* prepared Co doped (i.e. 0–1.5 mol%) NBT through the hydrothermal method with an average particle size of 200 nm and found multiferroic behaviour at room temperature [16]. In our recent work, we have substituted 5 mol% Co in NBT prepared by a solid state reaction technique with ambient atmosphere sintering [17]. The substituted Co-ion stabilizes predominantly in the  $\text{Co}^{2+}$  state and incorporates into the NBT lattice at the Ti-site with  $R3c$  phase stabilization. This  $\text{Co}^{2+}$  functional center acts as an acceptor type doping and hardens (i.e. increases coercivity ( $E_C$ )) the system without any significant change in remanent polarization ( $P_r$ ) values. However, the intermediate antiferroelectric (AFE) ordering is found to be suppressed due to Co-substitution [17]. In all the above mentioned reports, the magnetic cation substitution in NBT systems shows enhanced ferro/piezoelectric and dielectric properties. However, a detailed structural analysis and structure property correlation are less exploited in magnetically diluted NBT. In addition, observations of multifunctional behaviour such as magnetic properties are also limited. Our recent findings as discussed above show significant hardening in NBT along with creation of oxygen vacancies [17], making the system more difficult to pole electrically. Hence, in order to reduce the oxygen vacancies we had sintered the 5 mol% Co substituted NBT samples (NBT-Co) under  $\text{O}_2$  atmosphere. But, we could observe significant phase segregation as evidenced from microstructural and XRD analysis. Therefore, we synthesized 2.5 mol% NBT-Co samples through  $\text{O}_2$  atm sintering and observed a single phase without phase segregation. Hence, in this present work, we have extensively studied structural, ferroelectric, dielectric and magnetic properties of the optimized 2.5 mol% Co-substituted NBT and discussed these in terms of structure property correlation. This paper is organized as follows: the experimental details are given in section 2. The observations and certain justifications are given in section 3. Discussion based on structure property correlation is given in section 4.

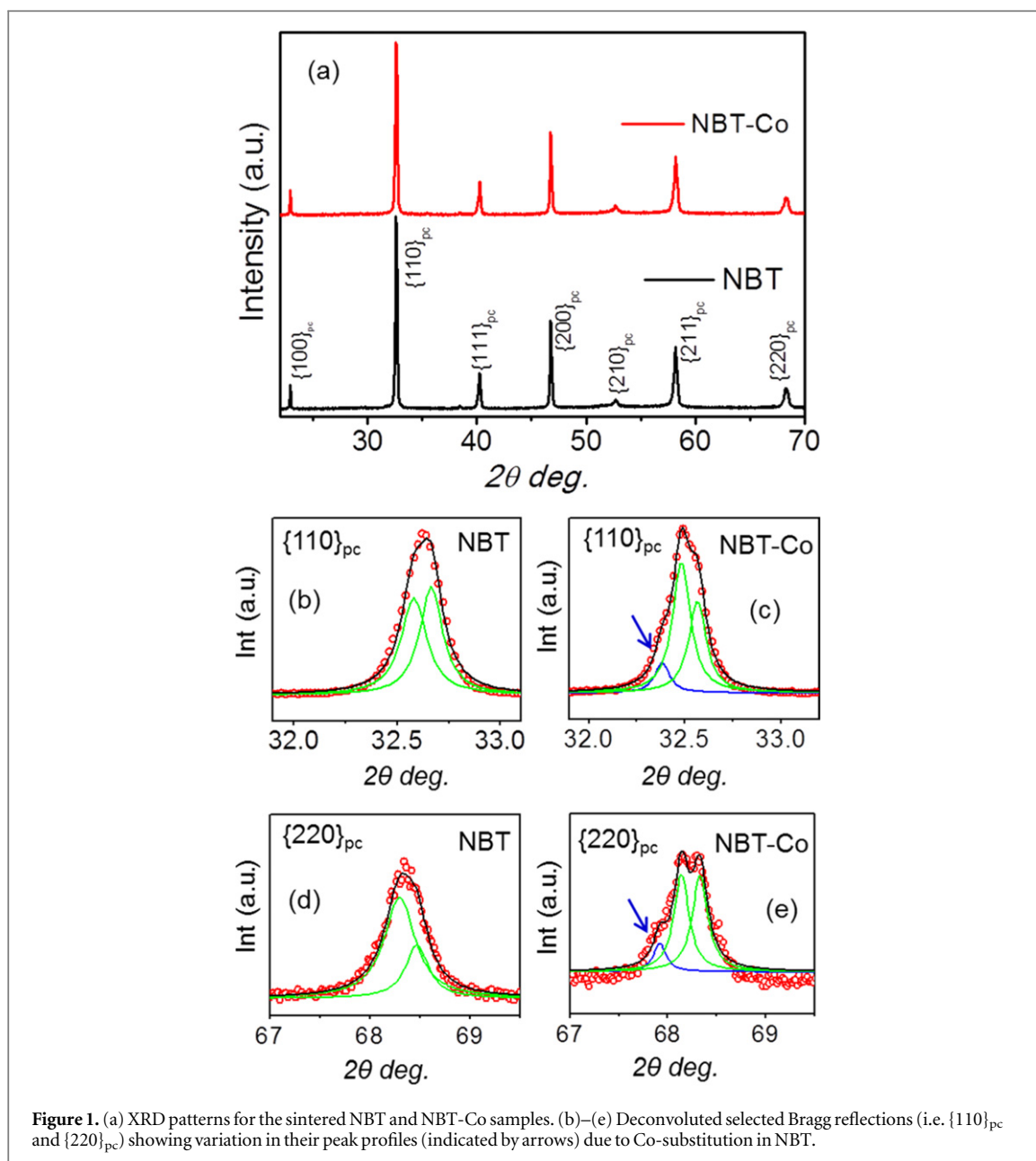
## 2. Experimental details

Polycrystalline NBT and  $\text{Na}_{0.5}\text{Bi}_{0.5}\text{Ti}_{0.975}\text{Co}_{0.025}\text{O}_{3\pm\delta}$  (NBT-Co) samples were prepared by oxygen ( $\text{O}_2$ ) atmosphere solid state sintering. High purity (99.99% from Sigma Aldrich, USA) dried  $\text{Na}_2\text{CO}_3$ ,  $\text{Bi}_2\text{O}_3$ ,  $\text{TiO}_2$  and  $\text{CoO}$  powders were used as precursors. Detailed synthesis procedure for NBT has been discussed in our previous work [18]. Stoichiometric precursors for NBT-Co systems were mixed thoroughly and followed by calcination at  $800^\circ\text{C}/3 \text{ h}$ . The calcined powders were ball-milled in 2-propanol medium and the milled slurry was dried overnight at  $80^\circ\text{C}$ . After drying, 1 wt% polyvinyl alcohol was added as a binder to the dried powders. After proper mixing, these powders were sieved, granulated and finally pelletized. These pellets were dried at  $400^\circ\text{C}/60 \text{ min}$  for binder removal and then sintered at  $1100^\circ\text{C}/3 \text{ h}$  under oxygen ( $\text{O}_2$ ) atmosphere with a flow rate of  $\approx 1000 \text{ ml min}^{-1}$  in a tubular furnace. X-ray diffraction patterns of the sintered powders were collected using PANalytical X'pert-pro diffractometer equipped with a  $\text{CuK}\alpha$  source. Phase analysis of the XRD patterns was carried out by using FullProf software package [19]. Diffuse reflectance spectroscopy (DRS) on the powder samples were recorded using a UV–vis–NIR spectrophotometer (UV3600, Shimadzu). Microstructures of the sintered samples were observed using FE-SEM microscope (Supra-40, Carl Zeiss, UK).  $P$  versus  $E$  measurements were performed using TF-Analyzer 2000 (aixACCT systems, GmbH) on the silver electroded samples. High temperature dielectric measurements were carried out using a precision Impedance Analyzer (6500B, Wayne-Kerr, UK) with a heating rate of  $0.5^\circ\text{C min}^{-1}$ . Magnetization measurements were performed using PPMS with a VSM assembly (Dynacool, Quantum Design, USA) which has a resolution of  $2 \times 10^{-7} \text{ emu}$ .

## 3. Results

### 3.1. X-ray diffraction analysis

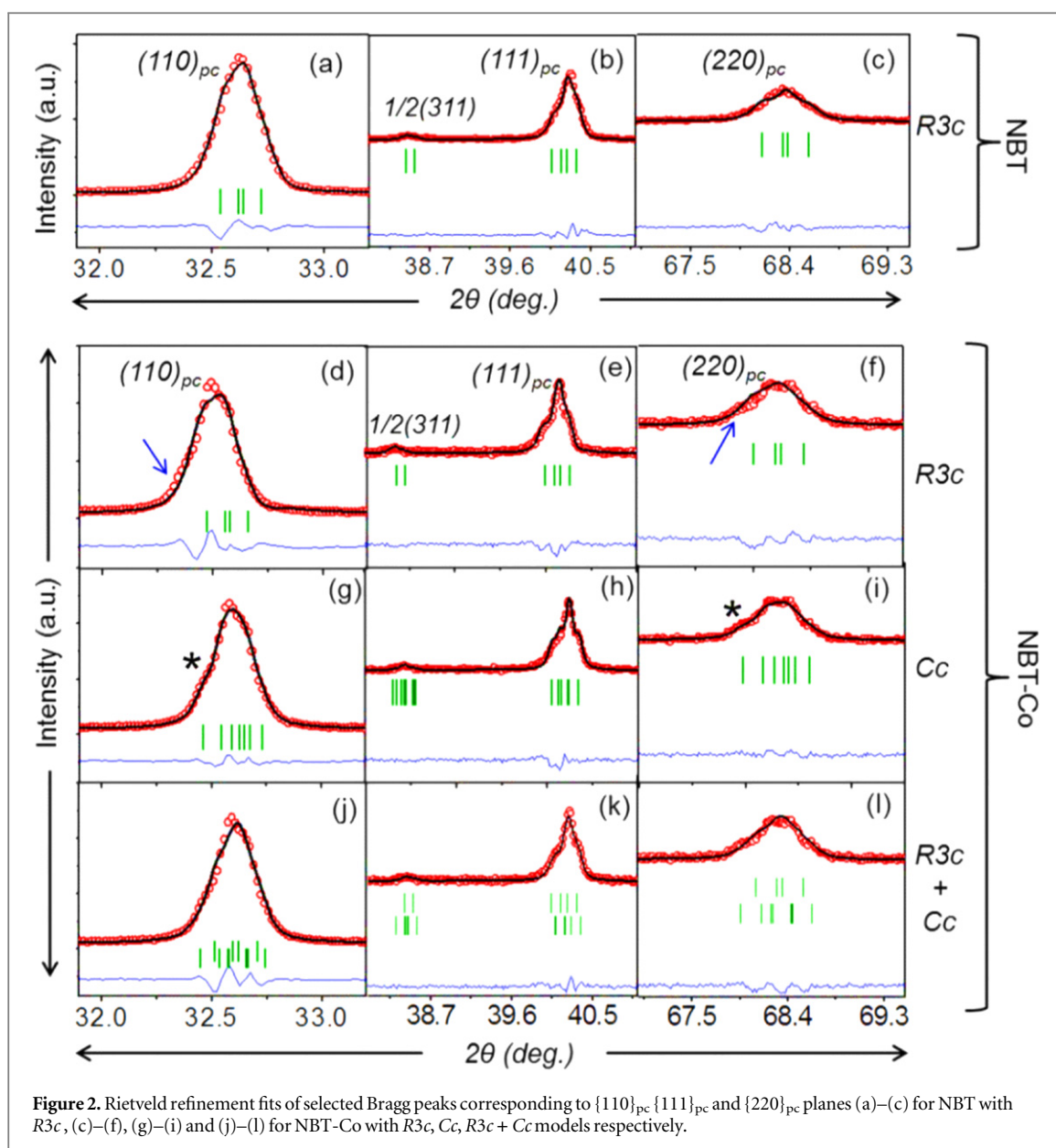
XRD patterns in the  $2\theta$  range from  $20^\circ$ – $70^\circ$  for sintered NBT and NBT-Co samples are shown in figure 1(a). The XRD pattern shows a complete perovskite structure formation with no detectable traces of secondary phases in both specimens. Further, close observation of certain Bragg reflections corresponding to  $\{110\}_{pc}$  in the angular range ( $2\theta$ ) between  $32^\circ$ – $33.5^\circ$  and  $\{220\}_{pc}$  (i.e.  $2\theta = 67^\circ$ – $69.5^\circ$ ) of NBT-Co system reveals an obvious change with three peak profiles rather than two as in NBT (see figures 1(b)–(e)). These changes indicate that Co-substitution in the host NBT lattice induces some structural variation. In order to analyse these variations, Rietveld refinement was carried out by considering  $R3c$  space group as a structural model for both the systems. Figures 2(a)–(f) show the selected Rietveld refined Bragg peaks corresponding to  $\{110\}_{pc}$ ,  $\{111\}_{pc}$  and  $\{220\}_{pc}$



planes for NBT and NBT-Co respectively, fitted by using  $R3c$  structural model. Both NBT and NBT-Co are found to be fitted well with the  $R3c$  Model. However, on close observation, the un-indexed Bragg positions were observed in  $\{110\}_{pc}$  and  $\{220\}_{pc}$  peaks of NBT-Co as indicated by arrows in figures 2(d) and (f). The aforementioned un-indexed Bragg positions as observed from the refined pattern are similar to those observed in the deconvoluted peak profiles of NBT-Co as shown in figures 1(c) and (e).

The observation of monoclinic  $Cc$  distortion is well documented in NBT [20, 21]. However, Rao *et al* reported the phase coexistence ( $R3c + Cc$ ) rather than  $Cc$  alone from synchrotron studies [22]. Dorcet *et al* justified the formation of tetragonal  $P4bm$  polar nano regions embedded in  $R3c$  matrix has been confirmed through TEM investigations in NBT [23]. Based on these symmetry criteria, we have refined NBT-Co using four structural models such as (i)  $Cc$ , (ii)  $Cm$ , (iii)  $R3c + Cc$  and (iv)  $R3c + P4bm$  respectively. In all the above mentioned models,  $Cm$  and  $R3c + P4bm$  show a poor fit with high  $\chi^2$  values. Hence,  $Cc$  and  $R3c + Cc$  models were chosen for further analysis. In order to provide an overall visual clarity and comparison, only selected Rietveld refined Bragg peaks have been shown on the magnified scale (see figure 2).

It is evident from the refinement that for NBT-Co system, both  $Cc$  and  $R3c + Cc$  models could fit satisfactorily the un-indexed Bragg position in  $\{110\}_{pc}$  and  $\{220\}_{pc}$  peaks as discussed earlier. In addition,  $Cc$  and  $R3c + Cc$  models fit the entire XRD pattern very well with nearly close goodness of fitting parameters such as  $R_p = 5.39$ ,  $R_{wp} = 6.88$ ,  $\chi^2 = 2.27$  for  $R3c + Cc$  and  $R_p = 5.20$ ,  $R_{wp} = 6.68$ ,  $\chi^2 = 2.20$  for  $Cc$  structural model respectively. Even though the fitting parameters are very close for both models, the shoulders (indicated by \*) in



$\{110\}_{pc}$ ,  $\{220\}_{pc}$  peaks and their corresponding peak profiles are fitted well with  $Cc$  rather than  $R3c + Cc$  (see figures 2(g) and (i)). From the above analysis,  $Cc$  space group is found to be a better structural model for the global average structure of NBT-Co system.

The entire refined pattern for NBT fitted with  $R3c$  and NBT-Co fitted with  $Cc$  is shown in figures 3(a) and (b). The refined atomic positions and other structural fitting parameters for NBT ( $R3c$ ) and NBT-Co ( $Cc$ ) are summarized in tables 1 and 2. Since isotropic displacement parameters (B) showed large values for Na/Bi, we refined anisotropic displacement parameters ( $\beta_{ij}$ ) for these atoms (see tables 1 and 2).

### 3.2. Microstructural analysis

Microstructures of the sintered NBT and NBT-Co samples are shown in figures 4(a) and (b). NBT has large densely packed equiaxed grains with an average grain size of  $14 \mu\text{m}$ . The NBT-Co sample shows a significant variation in the grain size and shape. It displays bi-modal grains with an average grain size of  $5 \mu\text{m}$ . However, phase segregation related to any parasitic phases is not observed at the grain boundaries of NBT-Co sample which in turn supports the solubility of Co-ion in the host NBT lattice.

### 3.3. Raman spectroscopy analysis

The global average structure and microstructural characteristics observed from XRD and FE-SEM, respectively, portray that substituted Co-ion in the host lattice induces structural distortions along with variations in the microstructure. Hence, in order to analyse the local structure variations in NBT-Co system, Raman

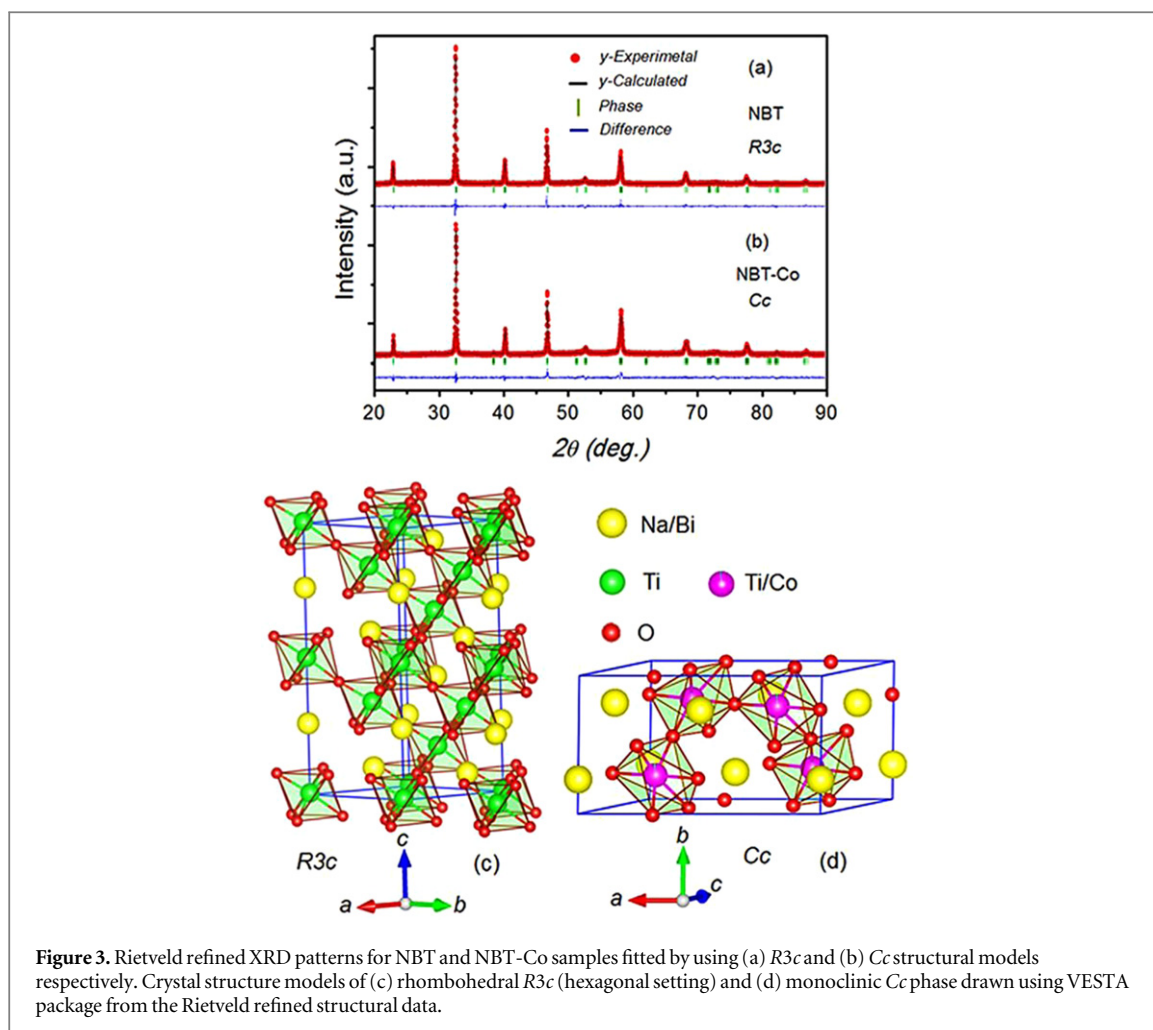


**Figure 3.** Rietveld refined XRD patterns for NBT and NBT-Co samples fitted by using (a)  $R3c$  and (b)  $Cc$  structural models respectively. Crystal structure models of (c) rhombohedral  $R3c$  (hexagonal setting) and (d) monoclinic  $Cc$  phase drawn using VESTA package from the Rietveld refined structural data.

**Table 1.** Structural parameters of NBT obtained by Rietveld analysis of x-ray powder diffraction data fitted with  $R3c$  model.

NBT: $R3c$				
Atom	x	y	z	B ( $\text{\AA}$ ) <sup>2</sup>
Na/Bi	0	0	0.2611 (2)	$\beta_{ij}$ (see below)
	$\beta_{11} = 0.0144$ (7); $\beta_{33} = 0.0023$ (2); $\beta_{12} = 0.0192$ (3)			
Ti	0	0	0.0063 (1)	0.103 (2)
O	0.1245 (6)	0.3298 (3)	0.0833 <sup>a</sup>	0.451 (5)

<sup>a</sup> = floating origin.

$a = 5.4826$  (3)  $\text{\AA}$ ;  $c = 13.4915$  (1)  $\text{\AA}$ ;  $V = 351.211$  (1)  $\text{\AA}^3$ .

$R_p = 7.97$ ;  $R_{wp} = 10.4$ ;  $\chi^2 = 1.66$ ;  $R_B = 3.79$ ;  $R_F = 3.39$ .

spectroscopy was used as a tool. Figure 5 shows the Raman scattering spectra for NBT which display four major broad intense bands designated as bands A to D. These broad bands for NBT are assigned to their corresponding phonon modes as per our previous theoretical calculations as follows [18]: the low frequency modes from  $109\text{--}134\text{ cm}^{-1}$  (Bi-O) and from  $155\text{--}187\text{ cm}^{-1}$  (Na-O) have been assigned to  $A_{\text{site-O}}$  ( $A_{\text{site}} = \text{Bi/Na}$ ) vibrations (band-A); the strong high intense band from  $246\text{--}401\text{ cm}^{-1}$  has been assigned to Ti-O vibrations (band-B); mid frequency vibrations from  $413\text{ cm}^{-1}$  are associated with  $\text{TiO}_6$  vibrations (band-C) and high frequency modes above  $\sim 700\text{ cm}^{-1}$  are assigned to oxygen displacements (band-D). In addition, the broad Raman bands in NBT and NBT-Co systems indicate the possible existence of both long and short range polar order [24]. A collective spectral change in terms of decrease in intensity in all major modes (i.e., band-A, band-B and band-C); subtle variation in the spectral profile in band-C (indicated by \*); increase in FWHM of  $\Delta\text{ cm}^{-1} \approx 25\text{ cm}^{-1}$  in band-C (i.e.,  $\text{TiO}_6$  octahedral mode) and minor frequency shifts in certain phonon modes in band-B and band-C (individual de-convoluted phonon modes are not shown here) indicate the presence of structural disorder in the

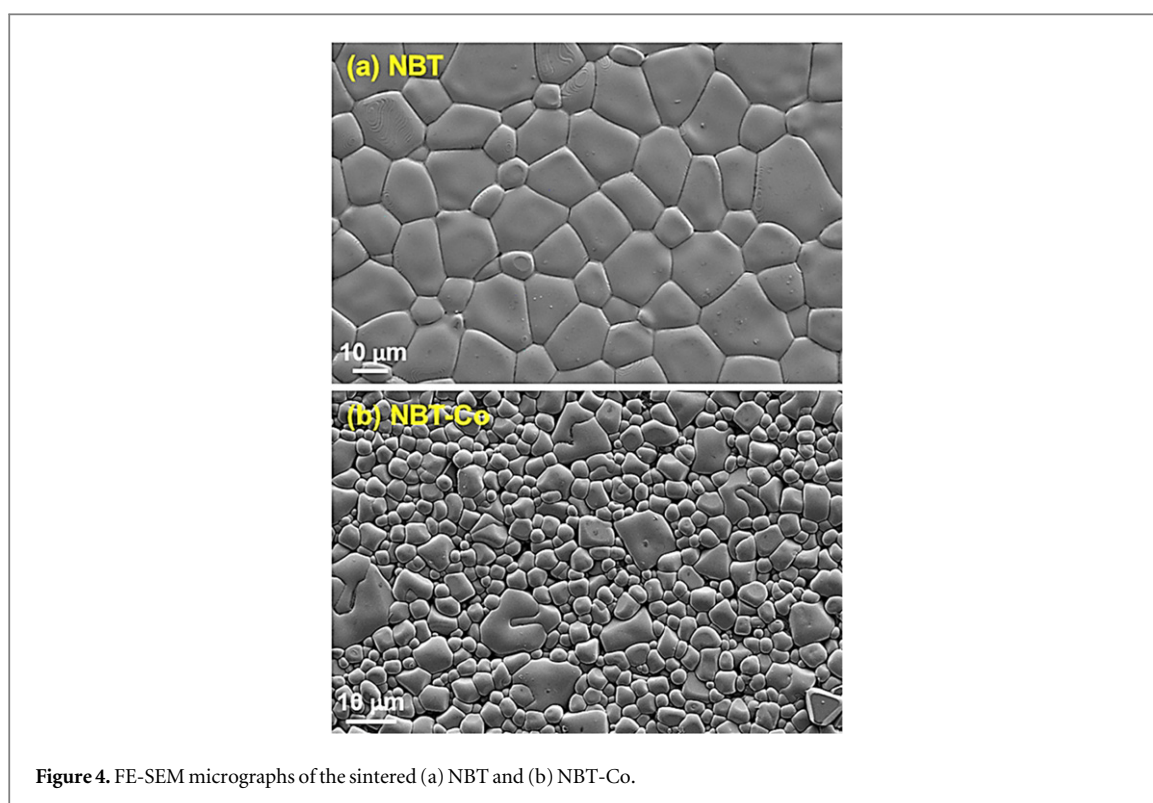
**Table 2.** Structural parameters of NBT-Co obtained by Rietveld analysis of x-ray powder diffraction data fitted with  $Cc$  model.

NBT-Co: $Cc$				
Atom	x	y	z	B ( $\text{\AA}$ ) <sup>2</sup>
Na/Bi	0	0.25	0	$\beta_{ij}$ (see below)
	$\beta_{11} = 0.0111$ (7); $\beta_{22} = -0.0120$ (7); $\beta_{33} = 0.0417$ (6) $\beta_{12} = 0.0064$ (3); $\beta_{13} = 0.0153$ (4)			
Ti/Co	0.2610 (1)	0.2485 (7)	0.7671 (1)	0.439 (3)
O1	0.0029 (8)	0.2424 (1)	0.4894 (3)	0.481 (4)
O2	0.1681 (1)	0.5013 (2)	-0.0792 (7)	0.481 (4)
O3	0.2595 (7)	-0.0073 (3)	-0.0010 (4)	0.481 (4)

$$a = 9.5150 (1) \text{ \AA}; b = 5.4809 (2) \text{ \AA}; c = 5.5117 (5) \text{ \AA};$$

$$\alpha = \gamma = 90^\circ; \beta = 125.285^\circ; V = 234.636 (7) \text{ \AA}^3;$$

$$R_p = 5.20; R_{wp} = 6.78; R_{exp} = 4.57; \chi^2 = 2.20; R_B = 4.48; R_F = 4.86.$$

**Figure 4.** FE-SEM micrographs of the sintered (a) NBT and (b) NBT-Co.

NBT-Co system due to Co-ion substitution [24]. In addition, a slight increase in intensity with a phonon shift towards lower frequency in band-D (see inset of figure 5—as indicated by arrow) suggests the presence of oxygen vacancies in the NBT-Co system, which presumably may be due to the mixed valence state of Co-ion [17].

### 3.4. UV–vis spectroscopy analysis

It is well known that the Co-ion can stabilize in multiple valence states such as  $2^+/3^+$ . Hence in order to visualize the possible valence states in the NBT-Co sample, solid state diffuse reflectance (DRS) UV–vis spectroscopy was carried out in this regard. DRS spectra (i.e.  $F(R) = (1-R)^2/2R$  ( $R$ —Reflectance)) measured as a function of wavenumber ( $\text{cm}^{-1}$ ) for NBT and NBT-Co samples are shown in figures 6(a) and (b). DRS spectrum for NBT (see figure 6(a)) depicts a linear absorption edge which indicates the absence of any crystal field (CF) transitions, because of their highly stable  $\text{Ti}^{4+}$ -ion (i.e.  $d^0$ -cation). However, a noticeable change in the nature of the DRS spectrum with two CF transitions for NBT-Co indicates the effect of Co-ion substitution in the host lattice (see figures 6(a) and (b)). Among the observed CF transitions, a weak shoulder centred around  $\sim 19\,200 \text{ cm}^{-1}$  could be attributed to a  ${}^4\text{T}_{1g} \rightarrow {}^4\text{A}_{2g}$  transition of  $\text{Co}^{2+}$  ( $d^7$ ) high spin (HS) ion complex [17].

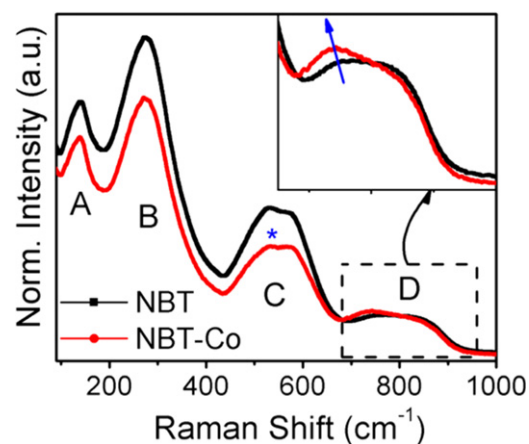


Figure 5. Raman scattering spectra for NBT and NBT-Co ceramics.

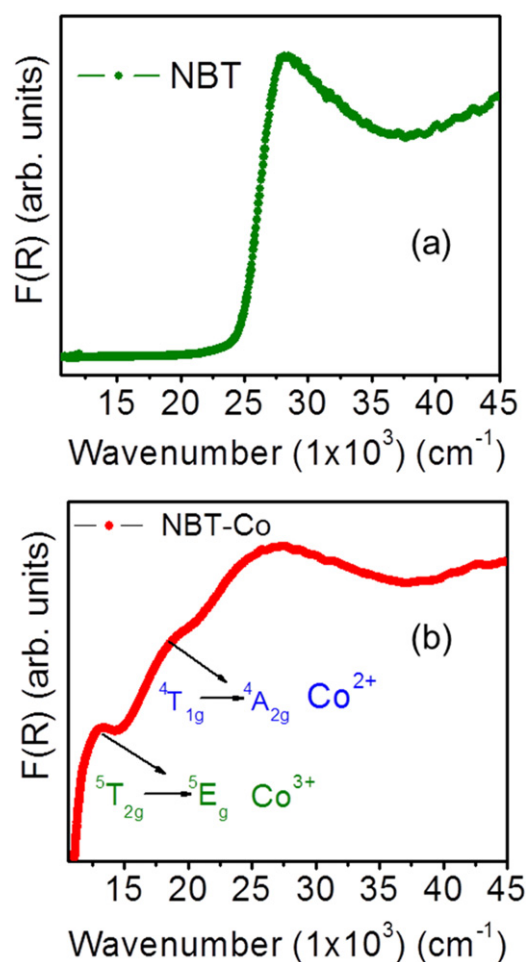


Figure 6. DRS UV-vis spectra for (a) NBT and (b) NBT-Co sample along with their corresponding crystal field transitions for  $\text{Co}^{2+}$  and  $\text{Co}^{3+}$ -ion.

The strong shoulder centred at  $\sim 14\,000\text{ cm}^{-1}$  could be assigned to the  ${}^5\text{T}_{2g} \rightarrow {}^5\text{E}_g$  transition of  $\text{Co}^{3+}$  ( $d^6$ -HS) ion. The intensity ratio as quantified from the de-convoluted CF-transitions (not shown here) supports the  $\text{Co}^{3+}$ -ion dominance in NBT-Co system. Most of the dominant CF transitions for a  $d^5$ -ion configuration lie well above  $20\,000\text{ cm}^{-1}$ , but we could not observe any signatures of  $\text{Co}^{4+}$ -ion ( $d^5$ -HS) CF-transitions in the NBT-Co spectrum. It is well known that Co in 4+ valence state is highly unstable, hence their stabilization is highly unfavourable in NBT-Co [25]. In addition, ionic radii of  $\text{Co}^{4+}$ -ion is  $0.53\text{ \AA}$  which is much smaller than

$\text{Ti}^{4+} = 0.605 \text{ \AA}$ ,  $\text{Co}^{2+} = 0.74 \text{ \AA}$  and  $\text{Co}^{3+} = 0.61 \text{ \AA}$ . In this regard, if there is a major stabilization of the  $\text{Co}^{4+}$ -ion, it will be reflected in the XRD pattern in terms of shift in  $2\theta$  positions which is not observed. All these aforementioned observations strongly support the absence of the  $\text{Co}^{4+}$ -ion in NBT-Co and confirm the stabilization of major  $\text{Co}^{3+}$ - and minor  $\text{Co}^{2+}$ -ion. Hence, further discussions in the subsequent sections will be discussed by considering mixed valence Co-ions in the NBT-Co system i.e.,  $\text{Co}^{3+}$  and  $\text{Co}^{2+}$ . The major  $\text{Co}^{3+}$ -ion stabilization in NBT-Co could be based on the processing conditions, which will be discussed as follows. During calcination at  $800 \text{ }^\circ\text{C}$  in ambient atmosphere, the reaction kinetics will strongly favour  $\text{Co}^{2+}$  stabilization as a similar observation was reported by Aksel *et al* in Mn substituted NBT systems [26]. The reaction kinetic in  $\text{Co}^{2+}$  can be represented using Kröger–Vink notation as  $\text{CoO} \xrightarrow{\text{TiO}_2} \text{Co}_{\text{Ti}}'' + \text{O}_{\text{O}}^\times + \text{V}_{\text{O}}^\bullet$  [17]. However, during sintering under  $\text{O}_2$  atm, oxygen vacancies get annihilated due to oxidation reactions as given by the equation  $\text{V}_{\text{O}}^\bullet + \frac{1}{2}\text{O}_2(\text{g}) \rightarrow \text{O}_{\text{O}}^\times + 2\text{h}^\bullet$  [26]. As a consequence, it leads to the stabilization of major  $\text{Co}^{3+}$  ion as per the reaction  $\text{Co}_{\text{Ti}}'' + \text{h}^\bullet \rightarrow \text{Co}_{\text{Ti}}'$  i.e.,  $(\text{Co}^{2+})\text{Co}_{\text{Ti}}'' \rightarrow \text{Co}_{\text{Ti}}'(\text{Co}^{3+})$  transformation. However, our experimental result shows that there may not be a complete transformation of  $\text{Co}^{2+}$  to  $\text{Co}^{3+}$ , but a major percentage of  $\text{Co}^{3+}$  formation takes place due to oxidation reactions. In this perspective,  $\text{Co}^{2+}$  and  $\text{Co}^{3+}$ -ions substituted at the  $\text{Ti}^{4+}$ -site of the host lattice act as an acceptor type doping, which may form two possible defect systems such as  $\text{Co}_{\text{Ti}}'' + \text{V}_{\text{O}}^\bullet \rightleftharpoons (\text{Co}_{\text{Ti}}'' - \text{V}_{\text{O}}^\bullet)^\times$  at the  $\text{Co}^{2+}$ -functional center (neutral defect dipole) and  $\text{Co}_{\text{Ti}}' + \text{V}_{\text{O}}^\bullet \rightleftharpoons (\text{Co}_{\text{Ti}}' - \text{V}_{\text{O}}^\bullet)$  at the  $\text{Co}^{3+}$ -functional centre (charged defect dipole) [17].

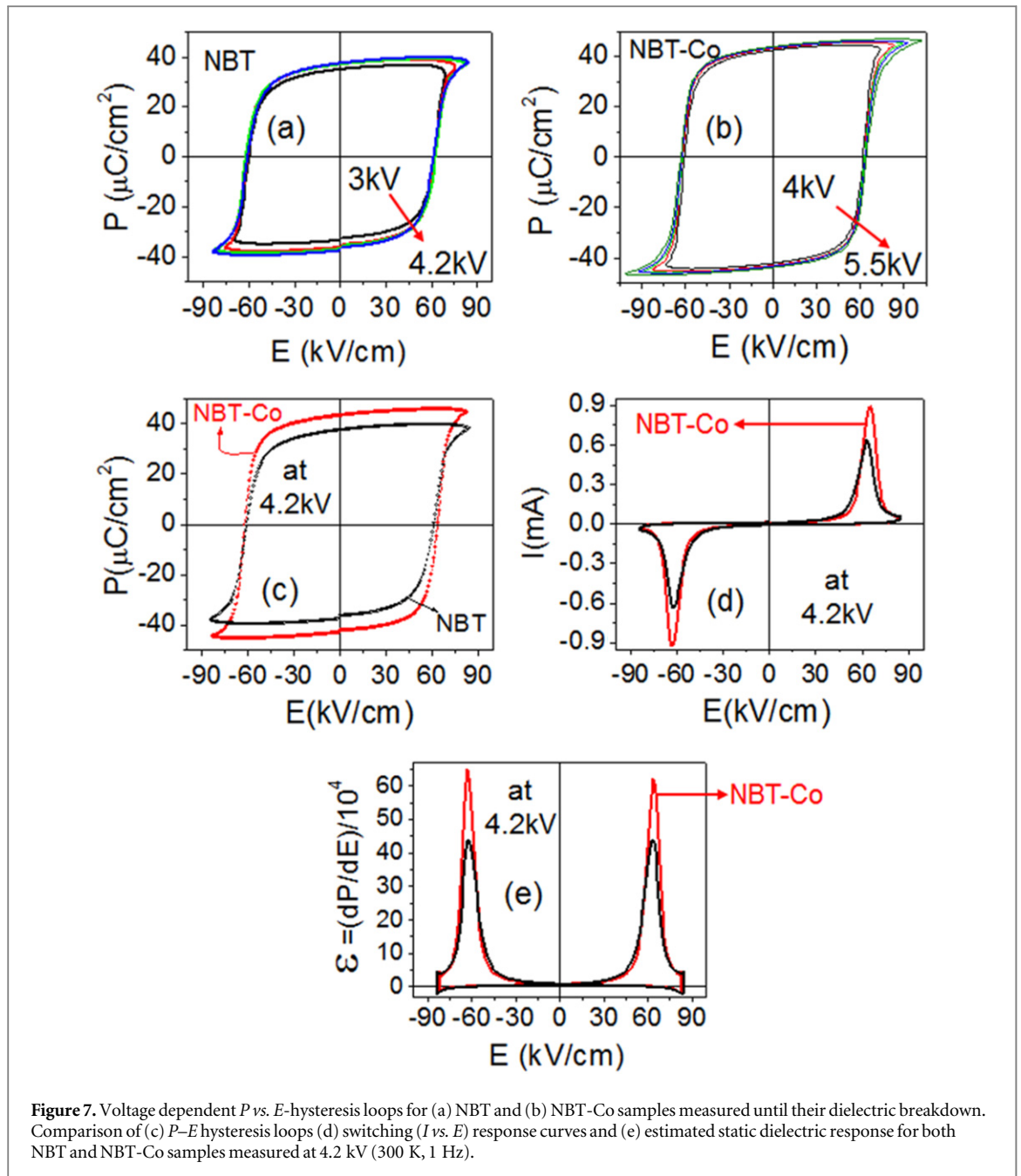
### 3.5. Ferroelectric properties

A voltage dependent polarization ( $P$ ) versus electric field ( $E$ ) hysteresis loop measured above 3 kV for both NBT and NBT-Co samples depicts well saturated and squared loops with high remanent polarization ( $P_r$ ) and coercivity ( $E_C$ ) values as shown in figures 7(a) and (b). The squareness of the  $P$ - $E$  loop can be quantitatively assessed by using an empirical relation:  $R_{sq} = (P_r/P_s) + (P_{1.1E_C}/P_r)$ , where  $R_{sq}$  is the squareness parameter of the hysteresis loop,  $P_r$  is the remanent polarization at  $E = 0$ ,  $P_s$  is the saturated polarization at some finite field strength below dielectric break down,  $P_{1.1E_C}$  is the polarization at field equal to  $1.1E_C$  [27]. The  $R_{sq}$  value is found to be  $\cong 2$  for both NBT and NBT-Co systems which indicates their strong ferroelectric (FE) character.

Interestingly, Co-ion substitution in the NBT-host lattice enhances the FE-ordering with a significant increase in  $P_r$ ,  $P_s$  values and area  $\langle A \rangle$  of the PE-loop (see table 3). However, no major change in  $E_C$  values was observed for the NBT-Co sample (NBT:  $\pm P_r/2 \cong 37.5 \mu\text{C cm}^{-2}$ ,  $\pm E_C/2 \cong 63 \text{ kV cm}^{-1}$ ; NBT-Co:  $\pm P_r/2 \cong 44 \mu\text{C cm}^{-2}$ ,  $\pm E_C/2 \cong 64 \text{ kV cm}^{-1}$  measured at 4.2 kV). In addition, a sharp switching current response for both the samples also indicates their intrinsic strong FE-character (see figure 7(d)). The unchanged  $E_C$  values in NBT-Co could be addressed due to the presence of dominant charged dipole  $P_D = (\text{Co}_{\text{Ti}}' - \text{V}_{\text{O}}^\bullet)$  (i.e. due to  $\text{Co}^{3+}$ ) rather than a neutral defect dipole  $P_D = (\text{Co}_{\text{Ti}}'' - \text{V}_{\text{O}}^\bullet)^\times$  (i.e., due to  $\text{Co}^{2+}$ ) which usually hardens the system by hindering the domain reversal [17]. The static dielectric response ( $\epsilon$ ) i.e.  $\epsilon = (dP/dE)/10^4$  estimated from the derivative of PE-loops [24] (see figure 7(e)) for the NBT-Co sample was found to be  $\cong 60$ , which is higher than NBT, i.e.  $\epsilon \cong 42$  (the static dielectric constant observed for NBT is close to the theoretically estimated value of 39.66).

### 3.6. Dielectric properties

Temperature (30–500  $^\circ\text{C}$ ) and frequency (5 kHz–1 MHz) dependence of the dielectric constant ( $\epsilon$ ) and loss tangent ( $\tan \delta$ ) for NBT and NBT-Co samples are shown in figures 8(a)–(d). It is evident from the dielectric plots that  $\epsilon$  for both the samples increases gradually with temperature until  $T_m$  (i.e. the transition temperature where the dielectric maximum occurs). Then after  $T_m$  (i.e.  $\sim$ above 300  $^\circ\text{C}$ ),  $\epsilon$  decreases until 500  $^\circ\text{C}$  corresponding to the paraelectric (PE) region [18]. However, a pronounced diffuseness near  $T_m$  was observed in the NBT-Co sample as compared to NBT. It is well known that  $(1/\epsilon)$  follows the Curie–Weiss law (i.e.  $\epsilon = C/(T - T_{CW})$  where  $T_{CW}$  is the Curie–Weiss temperature and  $C$  is the Curie–Weiss constant) in the PE regime for ideal ferroelectrics [18, 28]. However,  $(1/\epsilon)$  deviates from Curie–Weiss behaviour for both NBT and NBT-Co samples as seen in figures 8(b) and (d) which is one among the characteristics of relaxor ferroelectrics. Further, the temperature deviation ( $\Delta T_m$ ) i.e.,  $\Delta T_m = T_B - T_m$  ( $T_B$ – Burns temperature where  $1/\epsilon$  starts to follow Curie–Weiss law) was found to be about 70  $^\circ\text{C}$  and 90  $^\circ\text{C}$  for NBT and NBT-Co samples respectively. The deviation ( $\Delta T_m$ ) in the temperature dependent dielectric constant is due to the correlation degree among polar nano-regions (PNR) [28]. The degree of correlation can be estimated using the local order parameter ( $q$ ) which is based on a spin glass model as described through the equation:  $q(T) = (C - \chi(T - T_{CW})) / (C + \chi T_{CW})$  where  $\chi$  is the electrical susceptibility and  $q(T)$  is the local order parameter [28]. The  $q(T)$  represents the correlation degree of neighbouring cluster sized moment, i.e.,  $q = \langle P_i P_j \rangle^{1/2}$ , where  $P_i$  and  $P_j$  denote neighbouring cluster sized moments [29]. For both the samples, the  $q(T)$  is large below  $T_m$  and tails to zero well above  $T_m$  (see figure 8(e)), which indicates the existence of thermally stable short range PNR regions [29]. However, we noticed a variation in local order correlation strength between the NBT and NBT-Co sample in the region near  $T_{CW}$  and the region above  $T_m$ , i.e. in terms of variation in the slope  $dq(T)/dT$  (see figure 8(e)) and



their tailing effect as shown in figure 8(f). These aforementioned changes in the NBT-Co sample could be attributed to the effect of local dipolar interactions from the polar defect complexes (i.e.,  $P_D = (\text{Co}_{\text{Ti}} - \text{V}_{\text{O}})$  and  $P_D = (\text{Co}_{\text{Ti}}'' - \text{V}_{\text{O}})^{\times}$ ) and oxygen vacancies within the PNRs [29].

In addition, the order of diffusivity or disorderness in both samples has been analysed using modified Curie-Weiss law:  $1/\epsilon - 1/\epsilon_m = (T - T_m)^\gamma/C$  where  $\gamma$  is the diffusivity parameter [18]. The diffusivity parameter ( $\gamma$ ) can be calculated from the slope of  $\log(1/\epsilon - 1/\epsilon_m)$  vs.  $\log(T - T_m)$  plot as shown in the inset of figures 8(b) and (d). The  $\gamma$ -value for the NBT is 1.53 and 1.75 for the NBT-Co system.

### 3.7. Magnetic properties

Since Cobalt (Co) is a magnetically active cation, the magnetic properties of the NBT-Co system can be understood through magnetization measurements. In this perspective, zero-field cooled (ZFC)/field-cooled (FC) measurements were carried out in the temperature range from 10 K–300 K at 250 Oe as shown in figure 9(a). The ZFC/FC curves show magneto-thermal irreversibility with a small cusp (anomaly) around 45 K in the ZFC curve, which is not being observed in the FC curve (see figure 9(a)). This large bifurcation, cusp in ZFC and irreversibility in the ZFC/FC curves resembles a spin glass like behaviour [30]. In view of this context, magnetic field ( $H$ ) dependent ZFC/FC curves were recorded by varying the magnetic field from 250 Oe to

**Table 3.** Comparison of ferroelectric properties measured at 4.2 kV, static dielectric constant ( $\epsilon$ ) measured at 1 Hz (300 K) and relaxor features estimated from temperature dependent dielectric constant data (at 100 kHz) for NBT and NBT-Co systems.

Sample	$P_r$ ( $\mu\text{C cm}^{-2}$ )	$P_s$ ( $\mu\text{C cm}^{-2}$ )	$E_c$ ( $\text{kV cm}^{-1}$ )	$R_{sq}$	$\langle A \rangle$ ( $\text{CV cm}^{-3}$ )	$T_m$ ( $^\circ\text{C}$ )	$T_{CW}$ ( $^\circ\text{C}$ )	$\Delta T_m$ ( $^\circ\text{C}$ )	$\gamma$	$\epsilon_m$	$\epsilon$
NBT	37.5	39.3	63	$\cong 2$	11.5	310	210	70	1.53	2800	42
NBT-Co	44	45.2	64	$\cong 2$	13.4	295	190	90	1.75	3300	60

10 kOe. Interestingly, an H-dependent behavior was observed with a shift in the cusp (i.e.  $T_{\text{cusp}}$ ) towards low temperature with increasing magnetic field (H) (see figures 9(b)–(h)). The shift in  $T_{\text{cusp}}$  supports the presence of spin glass like behaviour in NBT-Co systems [30]. The inverse mass susceptibility ( $1/\chi_m$ ) plot with respect to temperature as derived from ZFC curves (not shown here) extrapolates to a negative temperature at  $1/\chi_m = 0$ . This feature indicates that NBT-Co system obeys the Curie–Weiss law (i.e.  $\chi = C/(T - \theta_{CW})$ ) but with a negative  $\theta_{CW}$  value which has been discussed in further section.

Co-ion substitution in the NBT host lattice displays a paramagnetic behaviour at room temperature as shown in figure 10(a). Further, to exploit these features magnetization ( $M$ - $H$ ) curves were measured from 300 K to 15 K. The  $M$ - $H$  plots show paramagnetic behaviour until 60 K and with decreasing the temperature below 50 K a non-zero coercive field ( $H_C$ ) and remanent magnetization ( $M_r$ ) values were observed along with non-saturating  $M$ - $H$  loops (see figure 10(b)). Figure 10(c) shows an increasing trend in  $M_r$  and  $H_C$  values with decreasing the temperature, which indicates the possibility of competing magnetic interactions in NBT-Co system.

## 4. Discussion

In recent years, structural ambiguities in NBT systems have been studied extensively. There has been a controversy over the room temperature structure of NBT between monoclinic ( $Cc$ ) and rhombohedral ( $R3c$ ) distortions. However, according to Rao *et al* the reported monoclinic ( $Cc$ ) distortion in NBT does not correspond to the room temperature thermodynamic equilibrium state. Rather, the observed global monoclinic ( $Cc$ ) distortion in the recent reports is attributed to the presence of  $\{100\}$  type nanotwins and strain heterogeneities which lead to the additional interference effects causing monoclinic like distortion as observed through x-ray/neutron diffraction techniques [1]. In addition, the theoretical predictions based on DFT and *ab initio* calculations also favour  $R3c$  phase [1, 18]. Hence, from the above discussions, we could justify the  $R3c$  phase being the equilibrium state for NBT at room temperature. Even though the  $R3c$  phase is found to be the stable equilibrium phase, chemical modifications/non-stoichiometry/defects can alter the  $R3c$  phase stabilization [21, 31]. In our present study, we have refined our XRD pattern for NBT by considering the  $R3c$  space group (see figure 3(a)). On analysing the structure of NBT-Co systems, the monoclinic distorted ( $Cc$ ) phase is found to be suited well as compared to the other structural models discussed in earlier section. The justifications for the monoclinic ( $Cc$ ) phase stabilization in NBT-Co are as follows: (i) a significant variation in the peak profiles with a shoulder on the lower angle side of both  $(110)_{\text{pc}}$  and  $(220)_{\text{pc}}$  planes (see figures 1(c)–(e)) strongly justifies the presence of structural distortion, (ii) the lower angle shoulders in  $(110)_{\text{pc}}$  and  $(220)_{\text{pc}}$  peaks could not be indexed with the  $R3c$  space group but eventually indexed and fitted well with the  $Cc$  space group (see figures 2(d)–(i)). The structural transition towards lower symmetric monoclinic structure ( $Cc$ ) could be due to the possibility of change in the tilt system from  $a^-a^-a^-$  to any one of these tilt systems (i.e.,  $a^-a^-c^0$ ,  $a^-a^-c^-$  and  $a^-b^-c^-$ ), along with a ferroelectric distortion with polarization vector confined in  $(1\bar{1}0)_{\text{pc}}$  plane [21, 31]. The significant change in the phonon modes as observed in terms of variation in the intensity, FWHM, and shifting and merging of certain  $\text{TiO}_6$  octahedral modes (band-C) in NBT-Co systems supports the possibility of variation in the tilt system as discussed in Raman analysis section (see figure 5).

The aforementioned discussions strongly favour the structural transition from  $R3c$  to monoclinic ( $Cc$ ) in NBT-Co systems. According to Vanderbilt and Cohen, there are three monoclinic phases based on their symmetry relationship with the parent phase [31]. The three phases are  $M_A$ ,  $M_B$  and  $M_C$  where  $M_A$  and  $M_B$  belong to the  $Cm/Cc$  space group while  $M_C$  belongs to the  $Pm$  space group [31]. Since NBT-Co stabilizes in the  $Cc$  space group we can conclude that it could stabilize either in the  $M_A$  or  $M_B$  phase (see figure 11(b)). The difference between the  $M_A$  and  $M_B$  phases lies in the magnitude of their polarizations. In the case of  $M_A$ ,  $P_X = P_Y < P_Z$ ; whereas for  $M_B$ ,  $P_X = P_Y > P_Z$ . From our observations, we found that  $a_m/\sqrt{2} > c_m$  for NBT-Co systems, where  $a_m$ ,  $c_m$  are the lattice constants obtained from the refined XRD data by considering the  $Cc$  model ( $a_m = 9.5150 \text{ \AA}$ ;  $a_m/\sqrt{2} = 6.7282 \text{ \AA}$ ,  $c_m = 5.5117 \text{ \AA}$  (see table 3)). This confirms that the NBT-Co system belongs to the  $M_B$  type monoclinic lattice [31]. The possible reasons for the monoclinic ( $Cc$ ) structural stabilization for NBT-Co systems are discussed subsequently.

The DRS UV–vis spectroscopic result portrays the presence of mixed valence Co-ions with a major  $\text{Co}^{3+}$  rather than  $\text{Co}^{2+}$  states in NBT-Co systems (see figure 6). The stabilized  $\text{Co}^{3+}$  ( $d^6$ -HS) and  $\text{Co}^{2+}$  ( $d^7$ -HS) ions

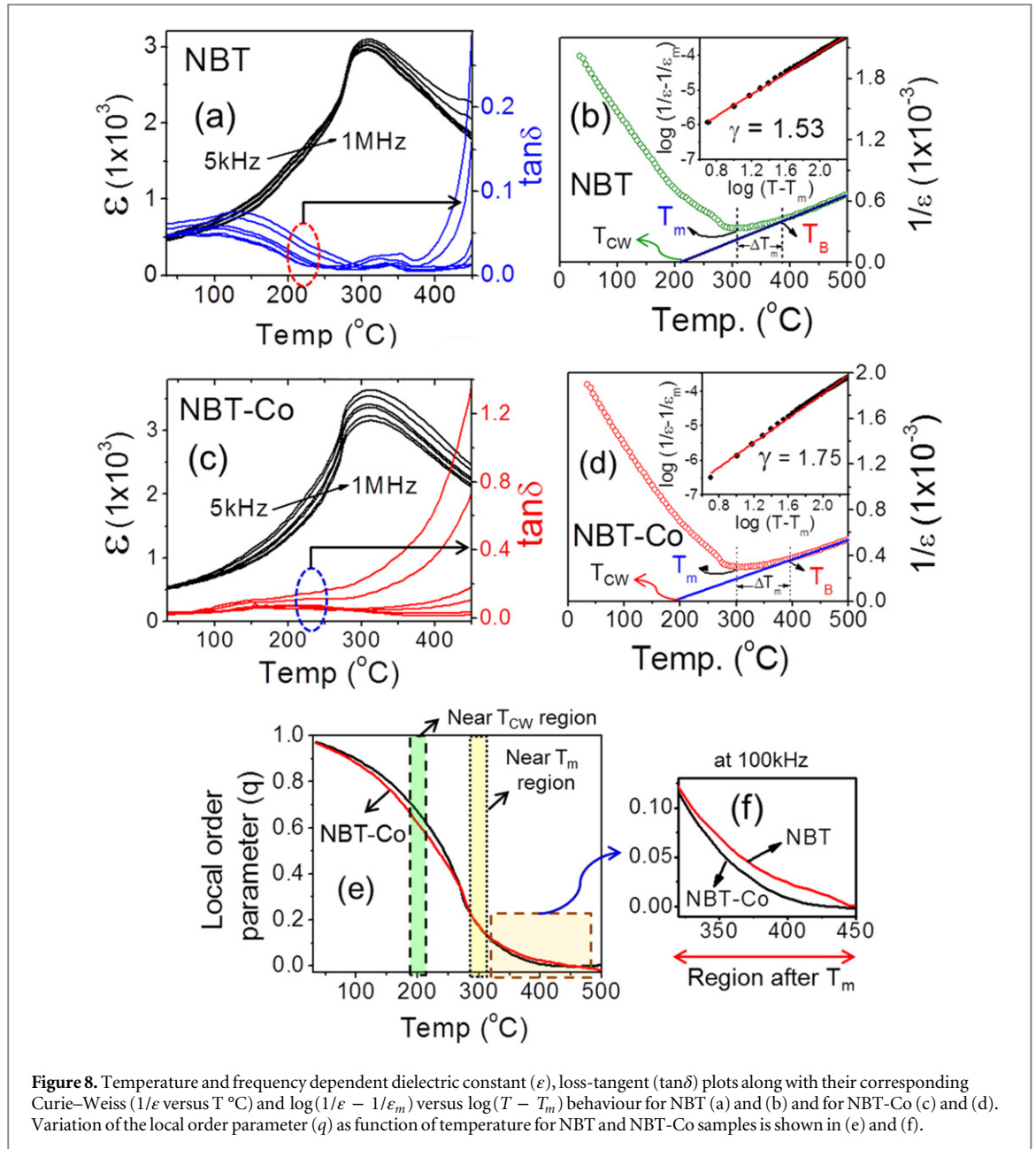
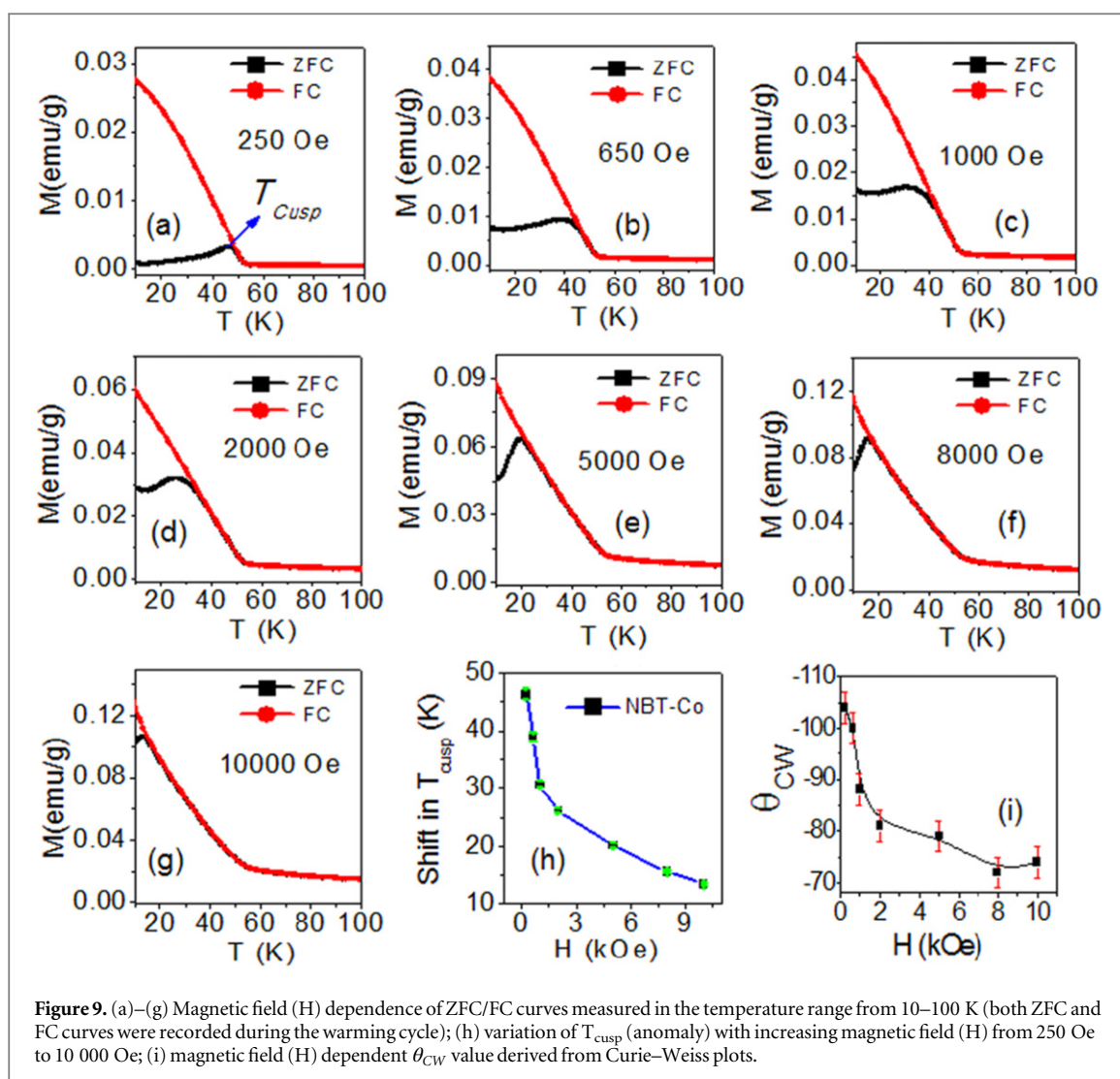


**Figure 8.** Temperature and frequency dependent dielectric constant ( $\epsilon$ ), loss-tangent ( $\tan\delta$ ) plots along with their corresponding Curie-Weiss ( $1/\epsilon$  versus  $T$   $^{\circ}\text{C}$ ) and  $\log(1/\epsilon - 1/\epsilon_m)$  versus  $\log(T - T_m)$  behaviour for NBT (a) and (b) and for NBT-Co (c) and (d). Variation of the local order parameter ( $q$ ) as function of temperature for NBT and NBT-Co samples is shown in (e) and (f).

are not a primary Jahn–Teller active ion [32]. However, the lattice crystal field of  $\text{Co}^{3+}$  and  $\text{Co}^{2+}$ -ions in NBT host lattices could couple with the orbital angular momentum ( $L$ ) and partially quench the orbital magnetic moment in  $t_{2g}$  states, which could give rise to spin–orbit-lattice stabilization (S-O) due to the presence of  $t_{2g}$  degenerate spin states [32]. As a result, there is a possible local elastic distortion with octahedral elongation along  $[111]$  at  $\text{Co}^{3+}$ -ion sites and octahedral compression along  $[001]$  at  $\text{Co}^{2+}$ -ion sites as shown in the schematic of figures 12(a) and (b).

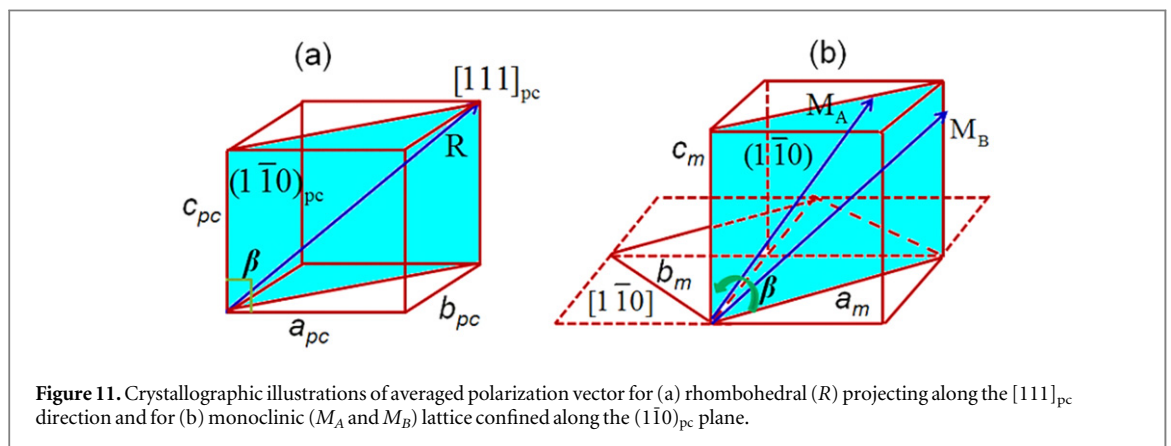
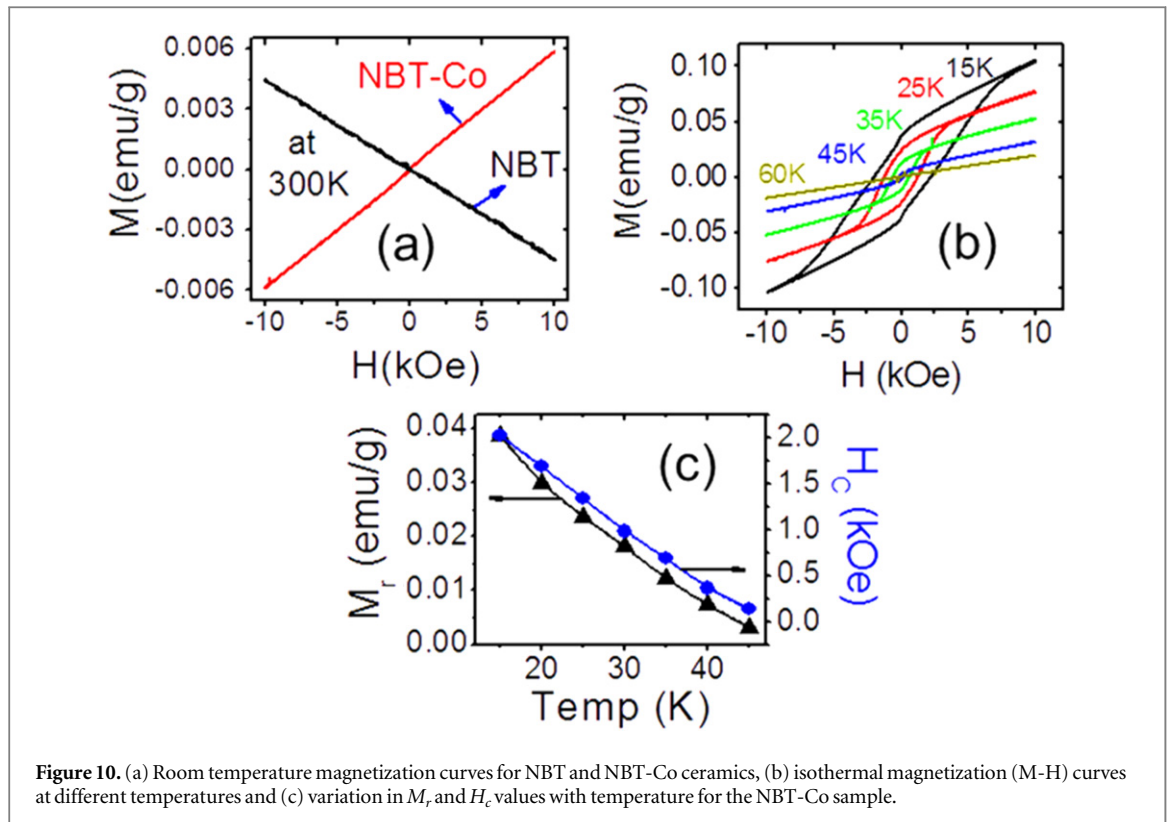
Hence, the S-O induced trigonal and tetragonal local site distortions can further reduce the symmetry and felicitate the octahedral tilt system crossover which leads to the stabilization of the lower symmetric  $Cc$  phase in NBT-Co systems. From the above discussions, we could justify the possible reasons for the stabilization of the  $Cc$  space group. An interesting feature in NBT-Co systems is the enhanced ferroelectricity with an increase in spontaneous polarization ( $P_s$ ) of about  $\cong 45.3 \mu\text{C cm}^{-2}$  as compared to NBT ( $P_s \cong 38.2 \mu\text{C cm}^{-2}$ ) (table 3). In conventional ferroelectrics, the direction of the polarization vector has a uniaxial constraint which is along  $[111]_{pc}$  and  $[001]_{pc}$ , in rhombohedral and in tetragonal symmetries respectively [33], whereas the monoclinic symmetry allows the polarization vector to rotate continuously within the  $(1\bar{1}0)_{pc}$  plane [31, 33]. This unique behaviour in monoclinic ( $Cc$ ) symmetry leads to the increase in an average net spontaneous polarization in NBT-Co systems [33]. Along with the increase in  $P_s$ ,  $P_r$  values, the enhanced relaxor feature is also a notable one. The enhanced relaxor feature (table 3) could be due to the pronounced B-site cation disorder which induces local microscopic compositional fluctuations as a consequence of Co-ion substitution [34]. In addition,



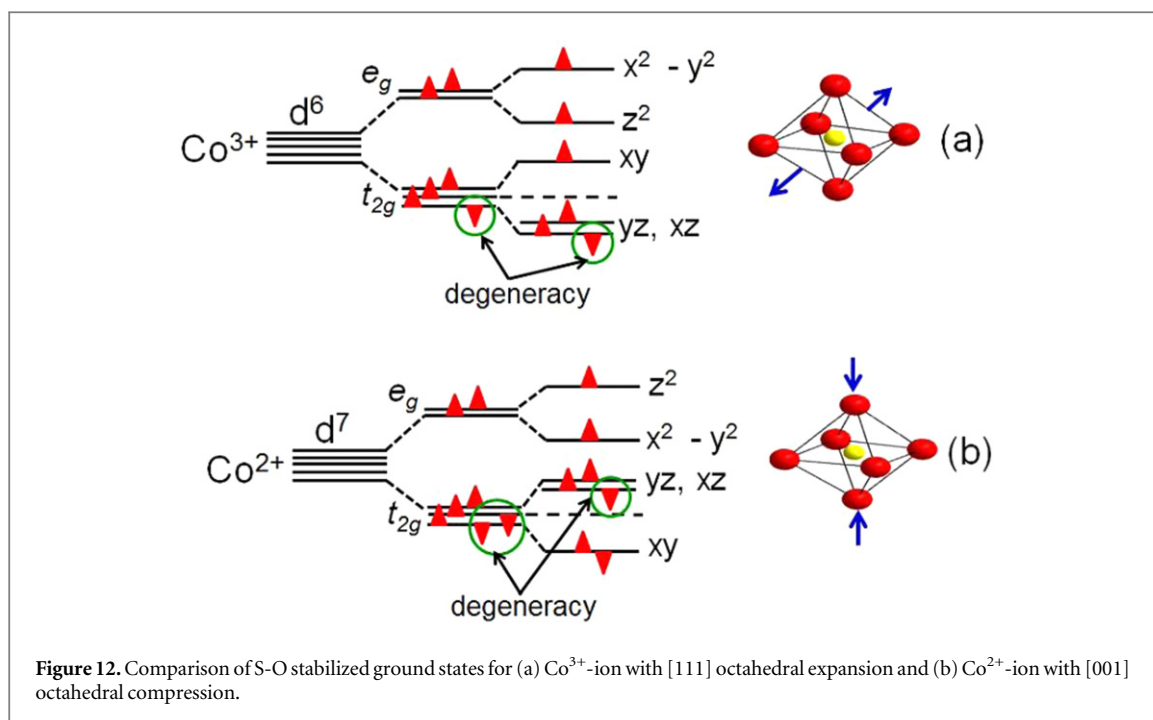
variation in the degree of short range correlation strength between polar nano regions (PNRs) also favours the enhanced relaxor feature [28, 29] (see figure 8). Along with the enhanced ferroelectric and relaxor feature, Co-ion substitution also displays a spin glass like behaviour as accounted in terms of the large bifurcation in ZFC/FC irreversibility curves and magnetic field (H) dependent shift in the  $T_{\text{cusp}}$  (see figure 9). However, a detailed focused study on the spin glass like feature in NBT-Co systems is required in order to conclude their exact nature. The negative  $\theta_{\text{CW}}$  value as observed from the inverse mass susceptibility plot ( $1/\chi_{\text{m}}$  versus T(K)) indicates the possibility of antiferromagnetic (AFM) exchange interaction persisting in the system [35]. A field dependent  $\theta_{\text{CW}}$  (see figure 9(i)) and non-saturating M-H along with loop opening are presumably accounted for due to the simultaneous existence of multiple Co-valence states which lead to competing AFM and ferromagnetic (FM) interactions [35]. The large coercivity ( $H_{\text{C}}$ ) value displayed below 30K from the M-H plots indicates an anisotropic character which could be partly due to high magneto-crystalline anisotropy of Co-ions (see figure 10(b)). The S-O stabilization as discussed above in  $\text{Co}^{2+}$  and  $\text{Co}^{3+}$ -ions can give rise to local magnetoelastic distortions in the presence of magnetic field (H), which becomes more effective especially at low temperatures (i.e., below 30 K), may also contribute to the high  $H_{\text{C}}$  values [32]. Thus, a multifunctional behaviour has been induced through Co-substitution in NBT along with enhanced ferroelectric and dielectric properties.

## 5. Conclusions

In summary, we conclude from our present work that a slight chemical modification with magnetic cation (i.e., Co-ion substitution of 2.5 mol%) in NBT systems could stabilize the monoclinic ( $Cc$ ) space group as their global



average structure. The effect of local distortions due to spin-orbit (S-O) stabilization in  $\text{Co}^{3+}$  and  $\text{Co}^{2+}$ -ion sites plausibly promotes the octahedral tilt crossover and hence stabilizes the  $Cc$  space group. The  $Cc$  lattice constants correlate well with the  $R$ -like ( $R$ -rhombohedral) distorted  $M_B$  phase, which has a polarization ( $P$ ) vector confined along the  $(1\bar{1}0)_{pc}$  plane. As a consequence, during polarization reversal the  $P$ -vector rotates freely and leads to the enhanced spontaneous polarization ( $P_s \cong 45.3 \mu\text{C cm}^{-2}$ ) in NBT-Co systems. Co-substitution at Ti-sites enhances B-site cation disorder and induces local microscopic compositional fluctuations, which in turn affect the degree of correlation strength between polar nano regions. These local variations give rise to enhanced relaxor features (i.e.,  $\gamma = 1.75$ ) in NBT-Co systems. Apart from the enhanced ferroelectric and relaxor characteristics, the presence of competing AFM and FM interactions due to mixed valence Co-ions leads to a spin glass like behavior especially below 50 K. All the above discussions based on structure-property correlation strongly portray the intrinsic character of NBT-Co systems rather than parasitic impacts. Further, it can be emphasized that the substitution of a magnetic cation in a non-magnetic ferroelectric system (i.e. diluted magnetic ferroelectrics) by proper processing conditions could induce the multifunctional behaviour with enhanced physical properties which is a legitimate temptation for the scientific community.



## Acknowledgments

The authors gratefully acknowledge the financial support of the Defence Research and Development Organization (DRDO), India under the project ERIP/ER/0900373/M/01/1430.

## References

- [1] Rao B N, Datta R, Chandrashekar S S, Mishra D K, Sathe V, Senyshyn A and Ranjan R 2013 *Phys. Rev. B* **88** 224103
- [2] Aksel E, Forrester J S, Nino J C, Page K, Shoemaker D P and Jones J L 2013 *Phys. Rev. B* **87** 104113
- [3] Jones G O and Thomas P A 2002 *Acta. Crystallogr. B* **58** 168
- [4] Chiang Y-M, Farrey G W and Soukhovjak A N 1998 *Appl. Phys. Lett.* **73** 3683
- [5] Kleemann W, Shvartsman V V, Bedanta S, Borisov P, Tkach A and Vilarinho P M 2008 *J. Phys.: Condens. Matter* **20** 434216
- [6] Shvartsman V V, Bedanta S, Borisov P, Kleemann W, Tkach A and Vilarinho P M 2008 *Phys. Rev. Lett.* **101** 165704
- [7] Shvartsman V V, Bedanta S, Borisov P, Kleemann W, Tkach A and Vilarinho P M 2010 *J. Appl. Phys.* **107** 103926
- [8] Valant M, Kolodiazhnyi T, Axelsson A-K, Babu G S and Alford N M 2010 *Chem. Mater.* **22** 1952
- [9] Valant M, Kolodiazhnyi T, Arcon I, Aguesse F, Axelsson A-K and Alford N M 2012 *Adv. Funct. Mater.* **22** 2114
- [10] Choudhury D *et al* 2011 *Phys. Rev. B* **84** 125124
- [11] Aksel E, Forrester J S, Kowalski B, Deluca M, Damjanovic D and Jones J L 2012 *Phys. Rev. B* **85** 024121
- [12] Davies M, Aksel E and Jones J L 2011 *J. Am. Ceram. Soc.* **94** 1314
- [13] Aksel E, Erdem E, Jakes P, Jones J L and Eichel R-A 2010 *Appl. Phys. Lett.* **97** 012903
- [14] Yao J, Ge W, Yan L, Reynolds W T, Li J, Viehland D, Kiselev D A, Kholkin A L, Zhang Q and Luo H 2012 *J. Appl. Phys.* **111** 064109
- [15] Ge W, Li J and Viehland D 2010 *J. Am. Ceram. Soc.* **93**[5] 1372
- [16] Wang Y, Xu G, Ji X, Ren Z, Weng W, Du P, Shen G and Han G 2009 *J. Alloys Comp.* **475** L25
- [17] Thangavelu K, Ramadurai R and Asthana S 2014 *AIP Advances* **4** 017111
- [18] Niranjana M K, Karthik T, Asthana S, Pan J and Waghmare U V 2013 *J. Appl. Phys.* **113** 194106
- [19] Rodrigues-Carvajal J 2000 *FULLPROF-A Rietveld Refinement and Pattern Matching Analysis Program* (France: Laboratoire Leon Brillouin, CEA-CNRS)
- [20] Aksel E, Forrester J S, Jones J L, Thomas P A, Page K and Suchomel M R 2011 *Appl. Phys. Lett.* **98** 152901
- [21] Rao B N and Ranjan R 2012 *Phys. Rev. B* **86** 134103
- [22] Rao B N, Fitch A N and Ranjan R 2013 *Phys. Rev. B* **87** 060102 (R)
- [23] Dorcet V and Trolliard G 2008 *Acta Mater.* **56** 1753
- [24] Fu J and Zuo R 2013 *Acta Mater.* **61** 3687
- [25] Lee J D 2012 *Concise Inorganic Chemistry* (Oxford: Oxford University Press) 5th edn
- [26] Aksel E, Jakes P, Erdem E, Smyth D M, Ozarowski A, van Tol J, Jones J L and Eichel R-A 2011 *J. Am. Ceram. Soc.* **94** 1363
- [27] Ma X, Yin J, Zhou Q, Xue L and Yan Y 2014 *Ceram. Intern.* **40** 7007
- [28] Viehland D, Jang S J, Cross L E and Wutting M 1992 *Phys. Rev. B* **46** 8003
- [29] Hong C-S, Chu S-Y and Hsu C-C 2010 *J. Appl. Phys.* **107** 094110
- [30] Guy C N, Tholence J L, Maletta H, Thouless D J, Hertz J A and Kirkpatrick S 1979 *J. Appl. Phys.* **50** 7308
- [31] Vanderbilt D and Cohen M H 2001 *Phys. Rev. B* **63** 094108
- [32] Dionne G F 2009 *Magnetic Oxides* (New York: Springer) pp 37–90
- [33] Priya S and Nahm S 2012 *Lead Free Piezoelectrics* (New York: Springer)
- [34] Uchino K 2010 *Ferroelectric Devices* (New York: CRC Press) 2nd edn
- [35] Durand A M, Belanger D P, Booth C H, Ye F, Chi S, Fernandez-Baca J A and Bhat M 2013 *J. Phys.: Condens. Matter* **25** 382203